

Comparisons of Calculations with PARTRAC and NOREC: Transport of Electrons in Liquid Water

Author(s): M. Dingfelder, R. H. Ritchie, J. E. Turner, W. Friedland, H. G. Paretzke, and R. N. Hamm

Source: Radiation Research, 169(5):584-594.

Published By: Radiation Research Society

DOI: <http://dx.doi.org/10.1667/RR1099.1>

URL: <http://www.bioone.org/doi/full/10.1667/RR1099.1>

BioOne (www.bioone.org) is a nonprofit, online aggregation of core research in the biological, ecological, and environmental sciences. BioOne provides a sustainable online platform for over 170 journals and books published by nonprofit societies, associations, museums, institutions, and presses.

Your use of this PDF, the BioOne Web site, and all posted and associated content indicates your acceptance of BioOne's Terms of Use, available at www.bioone.org/page/terms_of_use.

Usage of BioOne content is strictly limited to personal, educational, and non-commercial use. Commercial inquiries or rights and permissions requests should be directed to the individual publisher as copyright holder.

Comparisons of Calculations with PARTRAC and NOREC: Transport of Electrons in Liquid Water

M. Dingfelder,^{a,1} R. H. Ritchie,^b J. E. Turner,^c W. Friedland,^d H. G. Paretzke^d and R. N. Hamm^e

^a Department of Physics, East Carolina University, Greenville, North Carolina 27858; ^b 133 Normandy Road, Oak Ridge, Tennessee 37830; ^c 127 Windham Road, Oak Ridge, Tennessee 37830; ^d GSF – National Research Center for Environment and Health, Institute of Radiation Protection, D-85764 Neuherberg, Germany; and ^e 6800 Dorchester Drive, Knoxville, Tennessee 37909

Dingfelder, M., Ritchie, R. H., Turner, J. E., Friedland, W., Paretzke, H. G. and Hamm, R. N. Comparisons of Calculations with PARTRAC and NOREC: Transport of Electrons in Liquid Water. *Radiat. Res.* **169**, 584–594 (2008).

Monte Carlo computer models that simulate the detailed, event-by-event transport of electrons in liquid water are valuable for the interpretation and understanding of findings in radiation chemistry and radiation biology. Because of the paucity of experimental data, such efforts must rely on theoretical principles and considerable judgment in their development. Experimental verification of numerical input is possible to only a limited extent. Indirect support for model validity can be gained from a comparison of details between two independently developed computer codes as well as the observable results calculated with them. In this study, we compare the transport properties of electrons in liquid water using two such models, PARTRAC and NOREC. Both use interaction cross sections based on plane-wave Born approximations and a numerical parameterization of the complex dielectric response function for the liquid. The models are described and compared, and their similarities and differences are highlighted. Recent developments in the field are discussed and taken into account. The calculated stopping powers, W values, and slab penetration characteristics are in good agreement with one another and with other independent sources. © 2008 by Radiation Research Society

INTRODUCTION

A long-term goal of radiation research is to identify and trace all relevant events that happen from the time radiation first interacts with a biological target until an observable effect is produced. While this ideal is only partially realized at present, considerable progress has been made in the study of aqueous solutions of relatively simple organic molecules and structures irradiated by electrons. As described in the next section, the Monte Carlo technique offers a means to develop a literal stochastic computer simulation

of the detailed microscopic changes in targets as they actually unfold statistically upon irradiation. Monte Carlo track-structure codes using water in its different phases (vapor, liquid, ice) as a substitute for biological tissue have long been of interest. Early codes using water vapor [see e.g. refs. (1, 2)] and liquid water [see e.g. refs. (3, 4) and references therein] have been developed and compared [see e.g. ref. (5)]. Since then several codes based on these transport principles have been developed and frequently improved. A comprehensive study of track structure codes in radiation research can be found in a recent review article by Nikjoo *et al.* (6). Experimental measurements, whenever they are available, are used to test the quality of the computer models. Comparisons among different models and their underlying assumptions can also be useful in assessing the sensitivity of critical quantities that determine radiation action.

The first step in constructing such an electron track-structure simulation model is the determination of the partial attenuation coefficients, or inverse mean free paths, associated with the ionization, excitation and elastic-scattering processes of electrons in liquid water as functions of energy. While considerable experimental data are available for water vapor, measurements for the liquid present formidable problems and are largely lacking. Recently, two groups have completed a joint detailed study of their Monte Carlo computer models, developed independently, for calculating electron tracks in liquid water. It is instructive to compare the two approaches; the extent of the agreement in calculated quantities can provide some confidence in the results obtained. PARTRAC (7) was produced at the National Research Center for Environment and Health (GSF) and NOREC (4, 8) at the Oak Ridge National Laboratory (ORNL). The present paper compares the inverse mean free paths derived independently for liquid water for the two transport codes and the databases and theories on which they were developed. Figures showing all of these quantities are presented. In addition, W values, mass stopping powers, and slab-penetration curves, calculated with PARTRAC and with NOREC, are compared.

¹ Address for correspondence: Department of Physics, East Carolina University, Howell Science Complex, Greenville, NC 27858; e-mail: dingfelderm@ecu.edu.

TABLE 1
Ratios fi/ft of Ionizations to Total Events Obtained
from Total Cross Sections in NOREC and
PARTRAC

E (eV)	fi/ft		E (eV)	fi/ft	
	NOREC	PARTRAC		NOREC	PARTRAC
6.0	0.00	0.00	14.0	0.80	0.54
7.0	0.00	0.00	15.0	0.95	0.66
8.0	0.00	0.00	16.0	0.88	0.83
9.0	0.40	0.00	17.0	0.86	0.93
10.0	0.50	0.00	18.0	0.85	0.97
11.0	0.60	0.06	19.0	0.94	0.98
12.0	0.65	0.37	20.0	1.00	0.99
13.0	0.60	0.47			

MATERIALS AND METHODS

In principle, experiments with pencil beams of monoenergetic electrons normally incident on a thin absorber can be carried out to measure the inverse mean free paths needed for a computer simulation of an experiment. One measures the probability per unit distance traveled in the absorber that an electron will cause a certain quantum transition in the target while emerging within a particular solid angle and energy interval. Additional experimental information might be needed regarding the physico-chemical consequences of the affected target molecules. The complete set of such observed probabilities as functions of the incident electron energy comprise the inverse mean free paths needed for the computer simulation of the transport of an incident electron and its secondaries. The code randomly selects the individual events and reproduces statistically the results observed in the experiment. In essence, this describes the Monte Carlo method that is applied in PARTRAC and NOREC.

In practice, however, this approach presents formidable difficulties for liquid water because of the paucity of measured data needed as input for the model calculations. When NOREC and PARTRAC were developed, available data for the liquid came from three sources: optical reflection measurements for photons with energies from the infrared up to 26 eV (9), stopping-power measurements for energetic ions [see e.g. ref. (10) and discussion therein], and yields of hydrated electrons produced by high-energy electrons (11). As described below, these sources were used to help construct inverse mean free paths for liquid water, as were the much more extensive data for water vapor and ice. Calculations and extrapolations were made independently for PARTRAC and NOREC. As will be seen, the overall agreement on inverse mean free paths for liquid water between the two laboratories is quite good.

The dynamic properties of liquid water, including possible collective excitations, are described by its complex dielectric response function. This quantity can be written as the sum of its real and imaginary parts, $\varepsilon(\omega, k) = \varepsilon_1(\omega, k) + i\varepsilon_2(\omega, k)$, in which $E = \hbar\omega$ represents the energy transfer and the $q = \hbar k$ is the magnitude of the momentum transfer to the medium. It can be shown that, within the first-order plane-wave Born approximation, a fast but non-relativistic electron with speed v and kinetic energy $T = mv^2/2$, represented as a momentum eigenfunction and interacting with an infinite medium characterized by its response function $\varepsilon(\omega, k)$, will interact according to the doubly differential inverse mean free path,

$$\frac{d^2\Sigma}{d\omega dk} = \frac{2e^2}{\pi\hbar v^2} \frac{1}{k} \text{Im} \left[\frac{-1}{\varepsilon(\omega, k)} \right] = \frac{\hbar}{\pi a_0 T} \frac{1}{k} \text{Im} \left[\frac{-1}{\varepsilon(\omega, k)} \right]. \quad (1)$$

We shall use atomic units, i.e., to express lengths in units of the Bohr radius $a_0 = \hbar^2/me^2$ and energies in units of Hartrees; 1 Hartree = 2 Ry = me^4/\hbar^2 [m is the electron rest mass, e the elementary charge, and 1 Ry (Rydberg) the binding energy of hydrogen]. In atomic units, $e = \hbar = m = 1$, and the speed of light $c \approx 137$. It is assumed throughout that the response function depends only on the magnitude of the momentum trans-

TABLE 2
Energy Zone Splitting of Excitation Levels Used in
NOREC

Excitation level	Energy range (eV)
\bar{A}^1B_1	6.90–9.10
\bar{B}^1A_1	9.10–9.90
Ryd A+B	9.90–10.75
Ryd C+D	10.75–12.75
diffuse bands	12.75–14.75
plasmon	14.75–20.00

fer \vec{q} since the molecules of liquid water on average presumably are randomly oriented in space. In terms of scattering into the angle $d\theta$ at θ , the differential inverse mean free path is given by

$$\frac{d^2\Sigma}{d\omega d\theta} = \frac{4e^2}{\hbar v^2} G(\theta, \omega) \text{Im} \left[\frac{-1}{\varepsilon(\omega, k)} \right], \quad (2)$$

where

$$G(\theta, \omega) = \frac{\sqrt{T(T - \hbar\omega)} \sin\theta}{2T - \hbar\omega - 2\sqrt{T(T - \hbar\omega)} \cos\theta}. \quad (3)$$

The momentum transfer q and the scattering angle θ are related by

$$q = \hbar k = \sqrt{2m[2T - \hbar\omega - 2\sqrt{T(T - \hbar\omega)} \cos\theta]}^{1/2}. \quad (4)$$

The water molecule contains $Z = 10$ electrons which occupy 5 molecular orbitals (MO) named $1b_1$, $3a_1$, $1b_2$, $2a_1$ and the K shell of oxygen. Discrete electronic excitation levels are called \bar{A}^1B_1 , \bar{B}^1A_1 , Ryd A+B, Ryd C+D (Rydberg series), diffuse bands, and in the case of the NOREC model, plasmon, collective or dissociative excitation.

NOREC

1. Dielectric response function

Details of the construction of $\varepsilon(\omega, k)$ at ORNL, which underwent continual study and refinement over a number of years, are presented in the review paper by Ritchie *et al.* (4) and in publications cited therein. The original electron-transport code, called OREC, was renamed NOREC in 2003 after modifications were made for the treatment of elastic scattering and binary collisions (8). These changes did not affect $\varepsilon(\omega, k)$. Briefly, the optical reflection measurements (9) for photons with energies from the infrared up to 26 eV were used to plot the function $\varepsilon_2(\omega, 0)$, the imaginary part of the long-wavelength dielectric function. This curve was extended beyond the highest-energy data points to join smoothly with a curve representing the oscillator strength of the water molecule taken from ref. (12), the extension being constrained by sum rules. The entire quantity $\varepsilon_2(\omega, 0)$ was divided into three contributions: excitations, outer-shell ionizations and K-shell ionization, contributing 6.5%, 73.5% and 20% to the Bethe sum rule, respectively. Table 1 shows our assumptions for the ratio of the probability of ionizations fi to the total of ionizations plus excitations ft as a function of the energy transfer E . Each contribution was numerically fitted by a superposition of derivative Drude functions. In detail, the excitation contribution was fitted by 35 functions, while outer-shell and the K-shell ionizations were represented by 95 and 38 functions, respectively.² Then the excitation contribution was partitioned into the six different excitation levels considered by dividing the energy range into six consecutive energy intervals as shown in Table 2. The outer-shell ionization contribution was fractioned into four different molecular orbitals (MO) due to their contribution to the Bethe sum rule using ratios similar to water vapor. Numerical values are not provided for energies below 1 keV in this paper.² At energies above 1 keV, the following

² A file with numerical values for the Drude function parameters can be obtained from the authors upon request.

TABLE 3
Parameters a and b for the Partitioning Function
(see Text) of Ionizations into Different Molecular
Orbitals used in NOREC

MO	a	b
1b ₁	0.16	2.8×10^{-4}
3a ₁	0.11	9.7×10^{-4}
1b ₂	0.06	1.04×10^{-3}

partitioning functions were used: $f_{MO} = a \times \exp[-b(E - 1000)]$ for the three outermost different molecular orbitals and $f_{2a_1} = 1 - (f_{1b_1} + f_{3a_1} + f_{1b_2})$ for the 2a₁ orbital. The constants a and b are displayed in Table 3; the energy transfer E is used in eV.

The *derivative* Drude function is related to (but not the exact differentiation of) the Drude response function of classical (and quantal) matter; it has similar convenient analytical properties like normalization and Kramers-Kronig relationships, and the energy moment integrals show convergence properties similar to that of the exact atomic ground-state dielectric function. It has the following analytical form:

$$f_D(\omega, \gamma_n, \omega_n) = \frac{2\gamma_n^3\omega^3}{[(\omega_n^2 - \omega^2)^2 + \gamma_n^2\omega^2]^2}, \quad (5)$$

with fitting parameters ω_n and γ_n . The real part of the dielectric function $\varepsilon_1(\omega, 0)$ is then calculated analytically using the Kramers-Kronig relationships, Eq. (13).

2. Finite momentum transfer

Extrapolation of $\varepsilon(\omega, 0)$ into the $\varepsilon(\omega, k)$ plane was carried out as follows:

(i) by replacing f_D with

$$f_k(k) = f_k[\exp(-a_k k^2) + b_k k^2 \exp(-c_k k^2)] \quad (6)$$

in the case of excitation levels k and with

$$f_j(k) = f_j \left(1 - \sum_{\text{exc } k} f_k(k) \right) / \left(1 - \sum_{\text{exc } k} f_k \right) \quad (7)$$

in the case of ionization shells. The sum runs over all excitation levels k . The parameters a_k , b_k and c_k were originally derived from experimental data on water vapor [see e.g. ref. (3) and references therein] and are given in Table 4.

(ii) for ionization shells by replacing ω_n with

$$\hbar\omega_n(k) = \hbar\omega_{n0} + \frac{(\hbar k)^2}{2m} \quad (8)$$

or in a relativistic generalization with $\hbar\omega_n = \hbar\omega_{n0} + \sqrt{(c\hbar k)^2 + (mc^2)^2} - mc^2$, where ω_{n0} are the values of the ω_n parameters fitted to the $\varepsilon(\omega, 0)$ data. In this way, the energy-loss function goes over into a Bethe ridge for large q . Also, a simple linear relationship $\gamma_n = \gamma_{n0} + \text{Ry} \cdot q$ was chosen, where γ_{n0} are the damping-parameter values fitted to the $\varepsilon(\omega, 0)$ data. Finally, measurements of the early time dependence of hydrated electron yields from electron irradiation of liquid water by energetic electrons were compared with predictions based on the model. Results were consistent with the assumption that all outer-shell ionizations in the liquid lead to the appearance of an H₂O⁺ ion and a secondary electron. Depending on the presumed transition, some excitation modes can also result in ionizations. The ORNL model also includes non-local transitions due to presumed collective effects estimated for liquid water (4). Figure 1 shows the modeled imaginary part of the dielectric function in the optical limit, $\varepsilon_2(\omega, 0)$, as used in NOREC and PARTRAC; PARTRAC is discussed in the next section. Displayed are the contributions from excitations and ionizations, and the sum of both (total). Figure 2

TABLE 4
Parameters for the Momentum Transfer
Dependence of Excitation Levels used in NOREC
and PARTRAC

k	a_k	b_k	c_k
1	3.82	0.0272	0.098
2	2.47	0.0295	0.075
3	2.47	0.0311	0.074
4	3.01	0.0111	0.765
5	2.44	0.0633	0.425
6	2.44	0.0633	0.425

shows the NOREC (panel b) and PARTRAC (panel a) approximations to the (momentum-dependent) energy-loss function, $\text{Im}[-1/\varepsilon(\omega, k)]$, or the Bethe surface, for liquid water. Plotted on a logarithmic scale, it displays the contributions from excitations and from processes in which valence and K-shell electrons are liberated into the continuum.

3. Differential inverse mean free path

We have taken partial differential inverse mean free path functions for ionization of the molecular orbital states and the contributions of each of the molecular fragments. Data from Siegbahn (13) and Tan *et al.* (14) have led to the following assumptions for condensed matter shifts in the threshold energies, as shown in Table 5. For comparison, the threshold energies of liquid water as used in PARTRAC and discussed later are also shown.

We used a semi-empirical scheme for correcting the differential inverse mean free paths for exchange effects. The details of the empirical exchange correction are described in the Oak Ridge National Laboratory Report ORNL-TM-5188 (15). In Eq. (II-22) of that report, a correction factor is developed that is in analogy to the exchange correction to the Mott formula for free-electron free-electron scattering. Still another factor is used to correct for the action of the exclusion principle for electrons

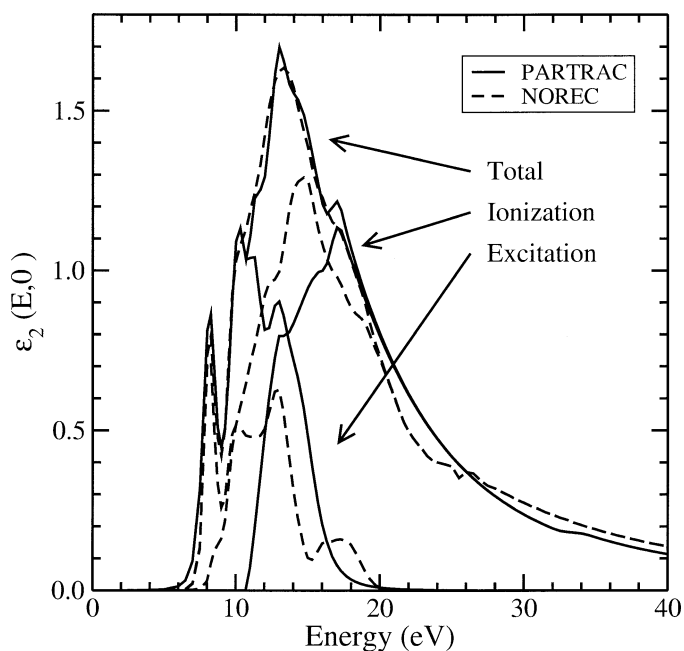


FIG. 1. Imaginary part of the dielectric response function in the optical limit, $\varepsilon_2(E, 0)$ as a function of the energy. Shown are the contributions from excitations and ionizations and the sum of both, as used in PARTRAC (solid lines) and NOREC (dashed lines).

scattered into the Fermi sea: It reduces the exchange correction at low energies and vanishes at the Fermi energy. There is no information on the effects of condensation into liquid from the isolated molecule on fragmentation processes. Led by measurements in the gas phase, we have assumed the channeling ratios shown in Table 6, regarded as constant at all electron-impact energies.

PARTRAC

1. Cross sections

Inelastic cross sections used in PARTRAC are based on a non-relativistic first-order plane-wave Born approximation and a model of the dielectric response function $\varepsilon(E, k)$ of liquid water as described below. Within the plane-wave Born approximation the doubly differential cross section is expressed as a product of the generalized oscillator strength or the (complex) dielectric response function of the medium under consideration and a purely kinematical factor representing the incoming electron. Practically, as in NOREC, the *inverse mean free path* or macroscopic cross section $\Sigma = N\sigma$ is used instead of the microscopic cross section σ . Here, N is the number density of the material under consideration. The energy differential inverse mean free path is then given by

$$\frac{d\Sigma}{dE} = \frac{1}{\pi a_0 T} \int_{k_{\min}}^{k_{\max}} \text{Im} \left[\frac{-1}{\varepsilon(E, k)} \right] \frac{dk}{k}. \quad (9)$$

In the PARTRAC approach we prefer to use the energy transfer E rather than the angular frequency ω as a parameter. However, in atomic units, the two quantities are identical. The integration limits k_{\min} and k_{\max} are given by

$$\begin{aligned} k_{\min} &= \frac{\sqrt{2m}}{\hbar} (\sqrt{T} - \sqrt{T-E}), \\ k_{\max} &= \frac{\sqrt{2m}}{\hbar} (\sqrt{T} + \sqrt{T-E}). \end{aligned} \quad (10)$$

Exchange is considered to be similar to NOREC (see above) in the sense of a semi-empirical scheme based on the Mott formula and described in detail elsewhere (4, 15). The exchange corrected differential inverse mean free path for a subshell j with binding energy E_j is given by

$$\begin{aligned} \frac{d\tilde{\Sigma}^j}{dE}(E, T) &= \frac{d\Sigma^j}{dE}(E, T) + \frac{d\Sigma^j}{dE}(T + E_j - E, T) \\ &\quad - \left(1 - \sqrt{\frac{E_j}{T}} \right) \left[\frac{d\Sigma^j}{dE}(E, T) \cdot \frac{d\Sigma^j}{dE}(T + E_j - E, T) \right]^{1/2}. \end{aligned} \quad (11)$$

The energy transfer ranges from $E_{\min} = E_j$ to $E_{\max} = (T + E_j)/2$.

At relativistic energies, the Bethe theory is used instead of the plane-wave Born approximation. In this theory, the differential inverse mean free path is given by

$$\frac{d\Sigma}{dE} = \frac{1}{\pi a_0 T^*} \left[A(E) \left(\ln \frac{\beta^2}{1 - \beta^2} - \beta^2 \right) + B^*(E) \right], \quad (12)$$

where $T^* = mv^2/2$ (not the kinetic energy) and $\beta = v/c$. $B^*(E) = B(E) + A(E) \ln(\hbar c/e^2)^2$, and $A(E)$ and $B(E)$ the Bethe coefficients as given by Dingfelder *et al.* (7). Both coefficients depend explicitly on the energy loss function $\text{Im}[-1/\varepsilon(E, k)]$.

At low incident electron energies (below 500 eV), an empirical correction factor $\Phi_j(T)$ based on experimental information obtained for water vapor and liquid water excitation/ionization energies is applied. Details can be found in Dingfelder *et al.* (7).

2. Dielectric response function

The complex dielectric response function fully describes the target material and depends only on the energy and momentum transfer E and $\hbar k$ and not on parameters of the incoming projectile. The dielectric function

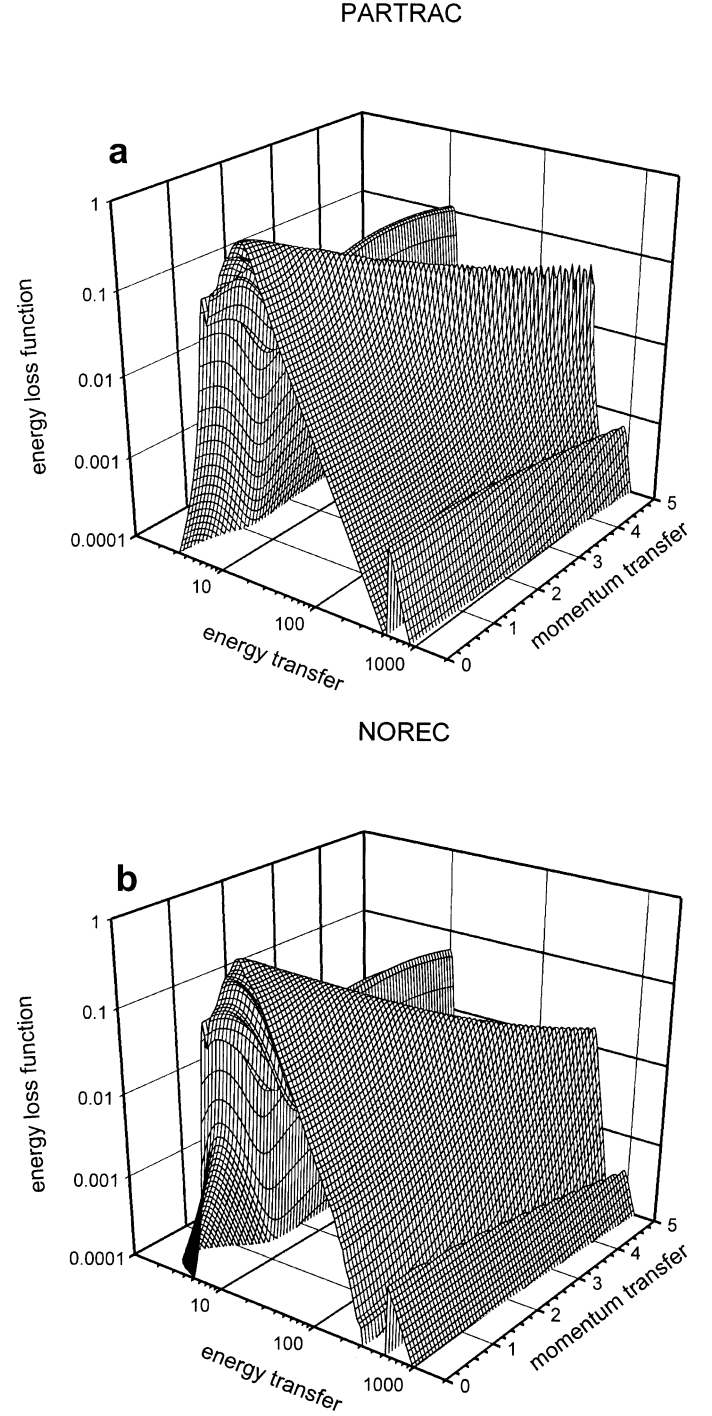


FIG. 2. The Bethe surface of liquid water, as used in PARTRAC (panel a) and NOREC (panel b). The energy transfer is given in eV, the momentum transfer in atomic units. Details are given in the text.

is a well-behaved complex function, and its real and imaginary parts are related by the Kramers-Kronig relations (16, 17)

$$\begin{aligned} \varepsilon_1(E, k) &= 1 + \frac{1}{\pi} P \int_{-\infty}^{\infty} \frac{\varepsilon_2(E', k)}{E' - E} dE', \\ \varepsilon_2(E, k) &= -\frac{1}{\pi} P \int_{-\infty}^{\infty} \frac{\varepsilon_1(E', k) - 1}{E' - E} dE', \end{aligned} \quad (13)$$

where P is the Cauchy principal value.

TABLE 5
Threshold (ionization) Energies E_k of Different Molecular Orbitals for the Gas and the Condensed Phase of Water, used in NOREC and PARTRAC

MO	E_k gas	E_k liquid	
		NOREC	PARTRAC
1b ₁	12.6 eV	8.0 eV	10.8 eV
3a ₁	14.7 eV	10.0 eV	13.4 eV
1b ₂	18.4 eV	13.0 eV	16.1 eV
2a ₁	32.2 eV	26.0 eV	32.2 eV
O 1s	539.7 eV	539.7 eV	539.0 eV

3. The optical limit

Our model of the dielectric function follows the general approach of Ritchie and coworkers (3, 4, 18) but introduces some improvements. Following the standard procedure, the imaginary part ε_2 of the dielectric function is modeled first in the optical limit, i.e., for momentum transfer $\hbar k = 0$ as a superposition of Drude-like functions. The use of Drude-like functions has the advantage that the principal value integrals of the Kramers-Kronig relations can be done analytically. This ensures an analytic and consistent dielectric function. We consider five different relevant excitation levels for liquid water (two electronic excitations: \tilde{A}^1B_1 , \tilde{B}^1A_1 ; two Rydberg series: Ryd A+B, Ryd C+D; and diffuse bands) and five ionization shells (1b₁, 3a₁, 1b₂, 2a₁, K shell of oxygen). We do not consider a plasmon excitation. Each discrete excitation is represented by a derivative Drude function,

$$D^*(E, E_k) = \frac{2f_k\gamma_k^3 E^3}{[(E_k^2 - E^2)^2 + \gamma_k^2 E^2]^2}, \quad (14)$$

and each ionization shell by an ordinary Drude function truncated and smeared out at the ionization energy,

$$D(E, E_k) = \int_{E_k - \Delta_k}^{E_k + \Delta_k} \frac{f_k \gamma_k E}{(\Omega^2 - E^2)^2 + \gamma_k^2 E^2} \exp\left(-\frac{(\Omega - E_k)^2}{2\Delta_k^2}\right) \Theta(E - \Omega) d\Omega. \quad (15)$$

The imaginary part $\varepsilon_2(E, 0)$ in the optical limit (i.e., $k = 0$) is then given by

$$\varepsilon_2(E, 0) = E_p^2 \left[\sum_{\text{exc } k} D^*(E, E_k) + \sum_{\text{ion } k} D(E, E_k) \right] \quad (16)$$

where E_p is the nominal plasmon energy. For liquid water, $E_p = 21.46$ eV. The parameters E_k , f_k , γ_k and Δ_k are obtained by a fit of ε_2 to the

TABLE 6
Fragmentation Channels of Excitation Levels and Percentages used in NOREC

Orbital	Fragmentation channeling
1b ₁	100% H ₂ O ⁺
3a ₁	100% H ₂ O ⁺
1b ₂	8% H ₂ O ⁺ , 70% OH ⁺ , 22% H ⁺
2a ₁	74% H ⁺ , 26% O ⁺

experimental optical reflectance data of Heller and coworkers (9) and other available experimental information as explained in detail elsewhere (7, 19). The real part ε_1 is then calculated by using the Kramers-Kronig relations. Consistency checks are done in calculating sum rules and other properties like the mean excitation energy I . The calculated value is $I = 81.8$ eV, which is slightly higher than the value of 75 ± 3 eV (20) adopted by the ICRU, but close to the new value of 79.75 ± 0.5 eV measured by Bichsel and Hiraoka (21). A detailed description of the fitting process and a discussion of the parameter can be found elsewhere (7, 19). Numerical values of the parameter used in our model are given in Table 7.

Finite Momentum Transfer

In general, the dielectric function depends on both energy transfer and momentum transfer. We introduce the momentum dependence in our model in allowing the parameter to depend on the momentum transfer $\hbar k$, i.e., replacing f_k , E_k and γ_k with the momentum-dependent functions $f_k(k)$, $E_k(k)$, and $\gamma_k(k)$, as suggested by Ritchie and coworkers (3, 4). We use Eq. (6) for $f_k(k)$ for excitation levels k and Eq. (7) for $f_j(k)$ for ionization shells j . Furthermore, for ionization shells j , E_j is replaced according to Eq. (8) in the Drude functions. In contrast to NOREC, no explicit momentum dependence is used for the width of the Drude functions, i.e., $\gamma_k(k) = \gamma_k$. This momentum dependence of the dielectric function creates a sharply peaked Bethe ridge with all its standard features in the sense of an impulse approximation as described elsewhere (7, 22) and displayed in Fig. 2a.

4. Simulation model

Fragmentation into the different excitation and ionization levels is obtained directly from the parameterization of the energy-loss function. It is assumed that outer-shell ionizations in the liquid lead to the appearance of an H₂O⁺ ion and a secondary electron. K-shell ionization leads to an H₂O⁺ ion, a secondary electron, and an additional Auger electron emitted from the outermost (1b₁) orbital. The electronic excitation level Ryd C+D (mean excitation energy 12.91 eV) leads to an autoionization of the 1b₁,

TABLE 7
Parameter of the Drude Model of the Dielectric Response Function of Liquid Water, Currently used in PARTRAC

k	Shells	E_{cut} (eV)	E_k (eV)	γ_k (eV)	Δ_k (eV)	f_k (eV) ⁻¹
1	\tilde{A}^1B_1	6.55	8.17	1.62	—	0.0118
2	\tilde{B}^1A_1	7.93	10.13	2.20	—	0.0230
3	Ryd A+B	9.21	11.31	2.10	—	0.01675
4	Ryd C+D	9.81	12.91	3.10	—	0.0285
5	diffuse bands	10.60	14.50	3.90	—	0.0280
6	1b ₁	10.79	11.95	12.50	1.16	0.1516
7	3a ₁	13.39	14.70	16.10	1.31	0.1222
8	1b ₂	16.05	16.60	19.40	0.55	0.2253
9	2a ₁	32.20	33.30	33.30	1.00	0.0826
10	K-shell	539.00	540.00	220.00	1.00	0.1608

Note. E_{cut} is the lower cutoff energy for excitations ($E_{\text{cut}} = E_k - \gamma_k$) in cross-section calculations and the ionization energy for ionizations ($E_{\text{cut}} = E_k - \Delta_k$), respectively.

orbital (ionization energy 10.79 eV) in 47.4%. Electronic excitations relax, decay or dissociate due to the scheme described in ref. (23) and are designed to ensure correct early prechemical and chemical stages of the water radiolysis.

NEW EXPERIMENTAL INFORMATION AND NEW MODEL CALCULATIONS

Increased interest and needs for radiation transport simulations in radiation biology and medical physics led to new experimental data in recent years. The Sendai group (24–27) determined the Bethe surface of liquid water, i.e. the energy-loss function $\text{Im}[-1/\varepsilon(E, k)]$, in the energy range up to 100 eV and momentum transfer range from 0.17 atomic units $< \hbar k < 3.59$ atomic units using inelastic X-ray scattering. This method, using high-intensity synchrotron radiation, measures the momentum and energy dependence of the energy-loss function for sufficiently large momentum transfers. They found, compared to a sharply peaked theoretical Bethe ridge (as shown e.g. in Fig. 2), a less pronounced and much more smeared out Bethe ridge. Dingfelder and Inokuti (22) showed that the Bethe surface of the PARTRAC model (Fig. 2a) contains all the basic features of the measured one. Hayashi *et al.* (26) extrapolated the energy-loss function to the optical limit, i.e. $k = 0$, and determined the real and imaginary parts of the optical dielectric response function $\varepsilon(E, 0)$ by Kramers-Kronig relations. This new data set agrees well with the optical reflectance measurements of Heller *et al.* (9) at energies below 7 eV and is systematically smaller for larger energies. This manifests itself especially in the maximum of the optical energy-loss function, where Hayashi's values are up to 30% smaller. This could be attributed to the fact that Heller *et al.* measured the optical reflectance on a liquid water surface that might have been contaminated by water vapor (26). However, both the NOREC and PARTRAC models of the optical energy-loss function show smaller values than those originally published by Heller *et al.*

Recently, Emfietzoglou and coworkers (28–30) presented different new models for the dielectric response function of liquid water based on the Sendai data. In a first step, Emfietzoglou and Nikjoo used an extended Drude model with their “D2” dispersion model, i.e., with momentum-dependent $f(k)$ and $E(k)$ parameters, similar to the PARTRAC model. They conclude that using the Sendai data rather than Heller's data leads to somewhat smaller inverse mean free paths at electron energies below several keV (28). In a second step, Emfietzoglou *et al.* extended their dispersion model to “D3”, i.e., allowing all three parameters $f(k)$, $E(k)$ and $\gamma(k)$ to be dependent on momentum, similar to the NOREC model (29, 30). They used a second-order polynomial for $\gamma(k)$, introduced an additional *retarding factor* in $E(k)$, and fitted their model to Sendai's experimental data in the (E, k) plane. They obtained a smeared-out and broadened Bethe ridge as seen in the experiment. They included a second-order Born correction (based on the Barkas effect and the optical energy-loss function) for energies $T > 100$

eV and a Mott-like exchange correction in the cross-section calculations. They found that the differential inverse mean free path at low incident electron energies (100 eV) shifts to smaller energy transfers. Also, their calculated stopping powers are significantly (up to 30%) smaller than those obtained by others authors in the energy range from 100 eV to 1 keV. A second independent measurement of the Bethe ridge would be very helpful to confirm these encouraging results.

Another area of interest is very low-energy (1–100 eV) electrons such as those found at the end of the tracks. It was generally believed that only energy depositions above the ionization thresholds lead to DNA single- or double-strand breaks. Therefore, both the NOREC and PARTRAC simulation models usually stopped electrons around an energy of 10 eV and considered them as solvated, or thermalized. In 2000 the Sherbrooke group (31) showed that electrons with energies well below ionization thresholds can cause single- and double-strand breaks in DNA through rapid decays of transient molecular resonances localized on the DNA's basic components. This can be obtained through electron attachment and dissociation reactions directly to the DNA or to the surrounding water shell and the subsequent reactions with the ions and radicals produced. Since then low-energy electron-driven damage to biomolecules remains of highest interest to investigators and has produced numerous publications, e.g. refs. (32–37). A review on this topic was published by Sanche in 2005 (38). Regarding electron transport in water, the Sherbrooke group (39) also measured integral scattering cross sections including elastic collisions, phonon excitations, vibrational excitations, electronic excitations and ionizations for low-energy (1–100 eV) electrons scattering in an amorphous-ice film and identified the 2B_1 transient anion state at around 5.2 eV. These cross sections are important in sub-excitation electron transport, i.e. in electron penetration ranges and low energies, as demonstrated elsewhere (40). Other reports include the trapping of 0–3 eV electrons in water ice (41) and secondary electron emission yields from thin amorphous-ice targets after fast proton impact.³ An extension of the electron transport below 10 eV is highly desirable for various applications in radiation biology.

RESULTS

Inverse Mean Free Paths

The total inverse mean free paths for ionization, excitation and elastic scattering in PARTRAC and in NOREC are shown in Fig. 3 as functions of electron energy. For elastic scattering, both simulation models use the cross sections for single atoms of hydrogen and oxygen from the National

³ C. I Christou, *Electron emission from condensed targets by 2-MeV proton impact*. Dissertation, East Carolina University, Greenville, NC, 2004. Available from ProQuest Digital Dissertations database (Publication No. AAT 3148836).

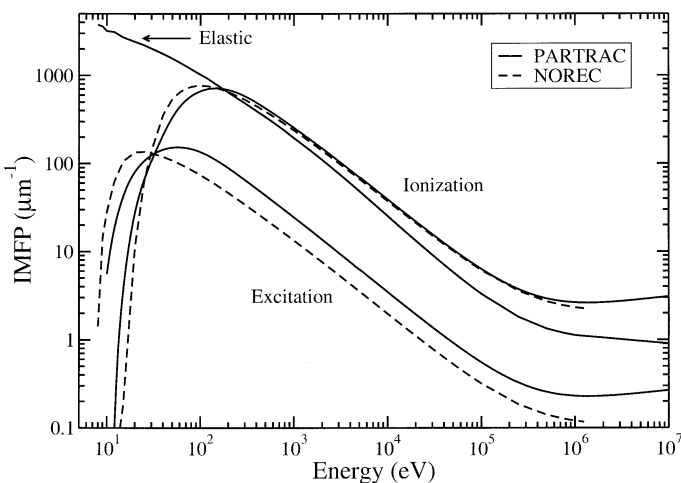


FIG. 3. Total inverse mean free paths (IMFP) for elastic scattering, excitations and ionizations as a function of the incident electron energy. Cross sections used in PARTRAC are represented by solid lines and those used in NOREC by dashed lines. Note that both codes use the same cross-section data sets for elastic scattering. Details are given in the text.

Institute of Science and Technology (NIST), given by Berger *et al.* (42) for electrons with energies down to 1 keV. Phase-shift calculations were made for lower energies and joined smoothly onto the NIST values at 1 keV. The threshold for electronic excitations is assumed to be 6.55 eV in PARTRAC and 7.4 eV in NOREC, while ionizations start at 8.0 eV in NOREC and at 10.8 eV in PARTRAC. The inverse mean free paths for ionizations of both models have approximately the same values, while inverse mean free paths for excitations of PARTRAC slightly exceed the values of NOREC.

The partial inverse mean free paths for the five ionization shells of the two models are shown in Fig. 4. Both models show very similar inverse mean free paths for the different outer ionization shells and use the same inverse mean free paths for the K shell of oxygen. The K-shell ionization cross section of oxygen used in both simulation models has been calculated using the distorted-wave Born approximation [as described by Segui *et al.* (43)] for energies up to 5 keV. Above this energy, the plane-wave Born approximation and the Bethe approximation described above were used. The partial inverse mean free paths for electronic excitations are shown in Fig. 5. Both models use a slightly different approach. PARTRAC considers only five electronic excitations, while NOREC considers these five electronic excitations plus a collective or dissociative excitation. In general, PARTRAC's inverse mean free paths are peaked at a slightly higher electron energy and appear broader compared to those for NOREC. In summary, in the NOREC model, outer-shell ionizations contribute 73.5%, the K shell of oxygen 20.0%, and excitations 6.5% to the Bethe sum rule. The PARTRAC model has contributions of 71.5%, 17.8% and 10.7%, respectively.

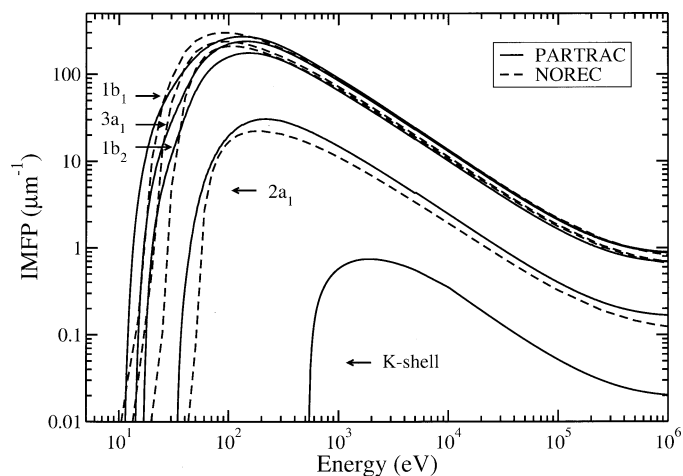


FIG. 4. Partial inverse mean free paths (IMFP) for the five ionization shells of liquid water as a function of the incident electron energy. PARTRAC and NOREC use the same K-shell ionization cross sections.

Differential Energy-Loss Inverse Mean Free Paths

Differential energy-loss inverse mean free paths for ionization are presented in Fig. 6. Shown are differential energy-loss inverse mean free paths for incident electron energies of 100 eV, 1 keV, 10 keV, 100 keV and 1 MeV. Note that the differential energy-loss inverse mean free paths are scaled by factors between 1 and 20,000 for better readability. Both codes use very similar differential inverse mean free paths for ionization. However, the ionization threshold is at 8.0 eV in the NOREC code and at 10.8 eV for PARTRAC. The maximum allowed energy transfer is $E_{\max} = (T + E_j)/2$ due to the exchange of electrons, as discussed earlier. The contribution from the oxygen K shell is clearly seen at an energy transfer around 540 eV.

Differential energy-loss inverse mean free paths for excitations are presented in Fig. 7. Again the differential en-

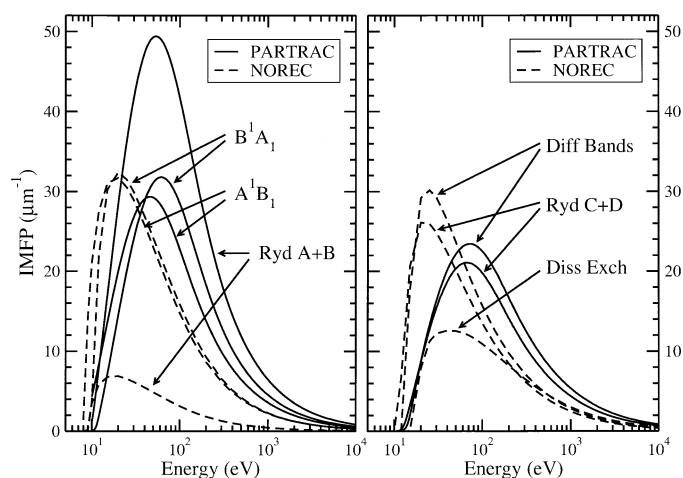


FIG. 5. Partial inverse mean free paths (IMFP) for electronic excitations of liquid water as a function of the incident electron energy. PARTRAC uses five electronic excitations while NOREC considers six. The inverse mean free paths are displayed on a linear scale.

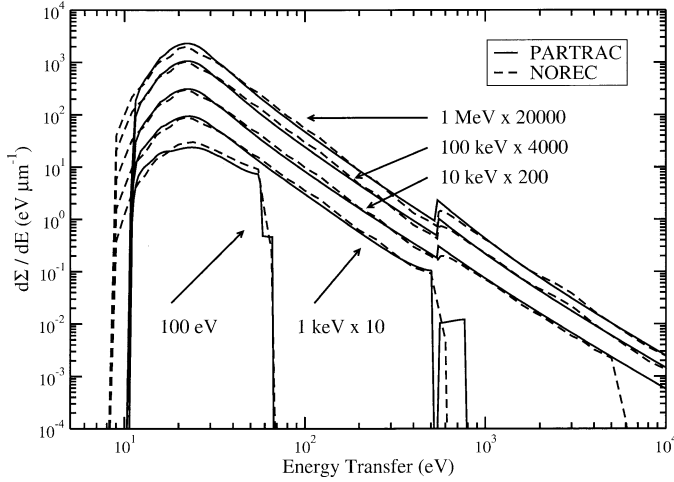


FIG. 6. Differential inverse mean free paths for ionizations as functions of the energy transfer for electron energies of 100 eV, 1 keV, 10 keV, 100 keV and 1 MeV. For better presentation, the curves have been multiplied by the constant factors as shown.

ergy-loss inverse mean free paths are shown for incident electron energies of 100 eV, 1 keV, 10 keV, 100 keV and 1 MeV. The *structures* seen in Fig. 7 originate from broadened and partially overlapping electronic excitations. NOREC (right panel) and PARTRAC (left panel) use slightly different partitioning of the energy-loss function into discrete excitation levels. PARTRAC uses an overlapping approach, while NOREC uses only slightly overlapping energy zones, as discussed earlier. This energy zoning leads to more pronounced sharp contributions from the different discrete excitation levels, as clearly seen in the right panel of Fig. 7. With further broadening and overlapping of excitation levels, these structures will eventually disappear, as clearly seen in Fig. 6 for (broad and overlapping) ionization levels.

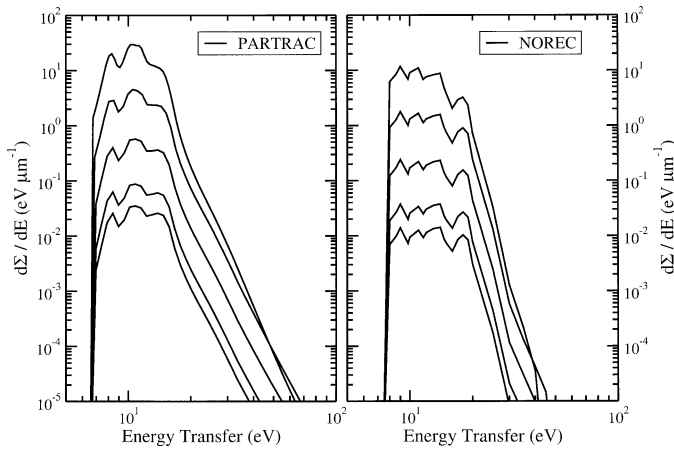


FIG. 7. Differential inverse mean free paths for excitations as a function of the energy transfer. The left panel presents cross sections used in PARTRAC, the right panel those used in NOREC. The curves correspond, from top to bottom, to incident electron energies of 100 eV, 1 keV, 10 keV, 100 keV and 1 MeV, respectively.

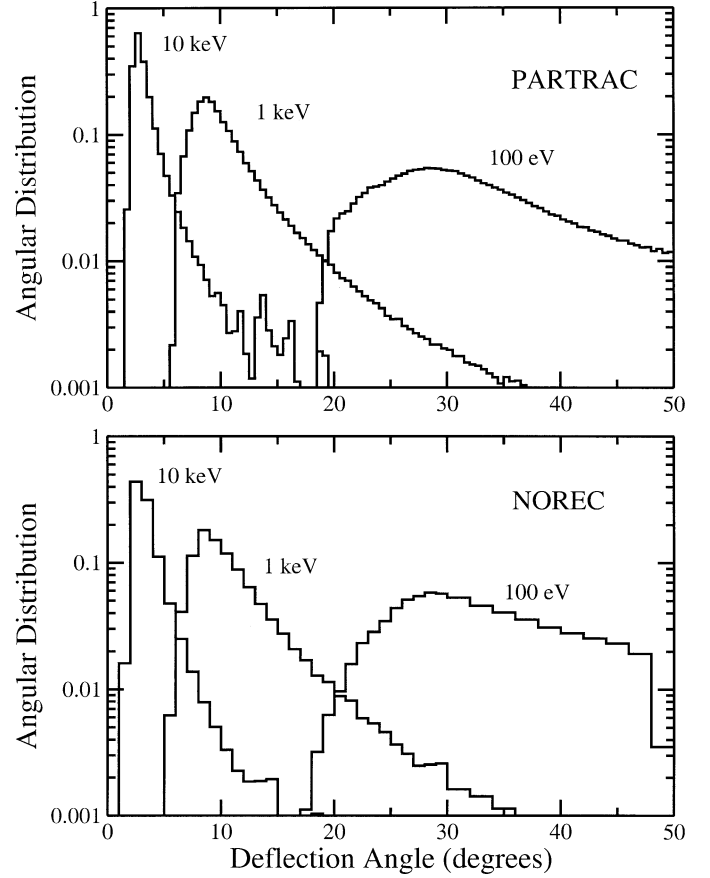


FIG. 8. Distribution of primary electron scattering angles in elastic and inelastic events as a function of the scattering angle. Simulated distributions from PARTRAC are presented in the top panel and those from NOREC in the bottom panel. Shown are distributions obtained from electrons with kinetic energy of 100 eV, 1 keV and 10 keV, respectively.

Angular Distributions

Angular distributions for inelastic scattering of the primary electrons are obtained from binary collision theory (classical deflection), as stated earlier. An electron with kinetic energy T experiencing an energy loss E scatters at an angle θ relative to its direction. The scattering angle θ for non-relativistic energies is given by

$$\cos \theta = \frac{T - E}{\sqrt{T(T - E)}} \quad (17)$$

and for relativistic energies by

$$\cos \theta = \frac{2T(T + 2mc^2) - 2E(T + 2mc^2)}{2\sqrt{T(T + 2mc^2)}\sqrt{T(T + 2mc^2) - 2E(T + mc^2) + E^2}} \quad (18)$$

The normalized angular distributions for scattering of primary electrons with kinetic energies 100 eV, 1 keV and 10 keV are shown in Fig. 8. At low incident energies this leads to a broad distribution of scattering angles. With increasing

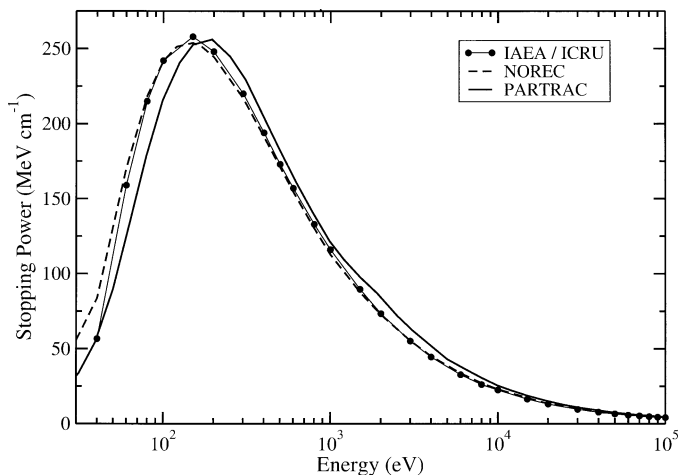


FIG. 9. Stopping powers for electrons in liquid water as a function of the electron energy. Results from PARTRAC (solid line) and NOREC (dashed lines) are compared with the IAEA/ICRU recommendations (20, 46) (symbols).

energies the distribution peaks (binary peak) in the forward direction (small scattering angles) and is virtually the same in both models. Secondary electron emission angles are modeled using the experimental data of Opal *et al.* (44, 45) for energy transfers $E < 100$ eV and the binary collision theory for energy transfers $E \geq 100$ eV. Non-relativistically, the secondary electron is emitted perpendicular to the scattered primary electron and at smaller angles toward forward direction at relativistic energies.

Stopping Power, W Values and Slab Penetration

To test the integrity and the implementation of the cross sections into the Monte Carlo simulation codes, some microdosimetric quantities have been simulated with the codes. Stopping power or the mean energy loss per unit track length was simulated by passing monoenergetic electrons through layers of liquid water and measuring their energy loss. The thickness of the layer was chosen to ensure a single collision environment, i.e., that the energy loss occurred in a single collision. This can be achieved by letting most of the electrons (99%) pass without a collision. The stopping powers of liquid water simulated with PARTRAC and with NOREC are shown together with the recommendations of the ICRU (20) (for energies >10 keV) and the compilation of the International Atomic Energy Agency (IAEA), ref. (46), Table 7.6 (for energies <10 keV) in Fig. 9. The agreement among the three independent assessments is good. The stopping power obtained from PARTRAC is shifted to somewhat higher energies compared to the IAEA compilation and the NOREC results. It should be noted that the stopping power was not used in the PARTRAC model to adjust parameters. It is the result of the best estimate of the energy-loss function and the resulting differential inverse mean free paths. The simulated stopping power agrees well with that calculated from the differential inverse mean free paths.

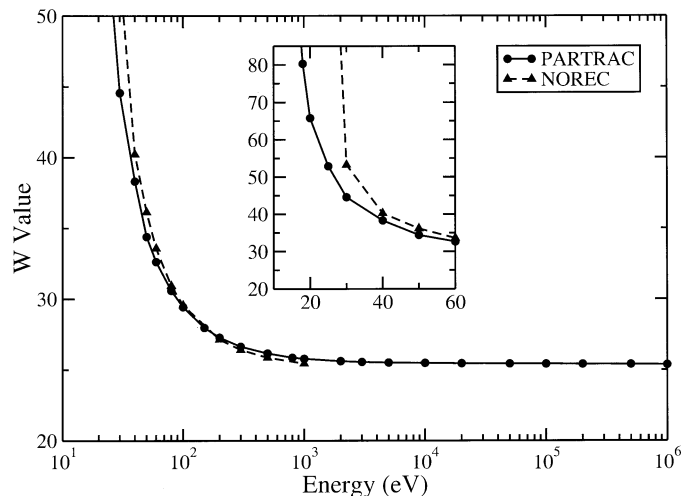


FIG. 10. W values obtained with PARTRAC (solid line) and NOREC (dashed line) as a function of the electron energy. The inset enlarges the low-energy region.

Another important microdosimetric quantity is the W value or the average energy needed in a gas to produce an ion pair. We use the same definition as in the gas (47) and calculate the W value of liquid water by dividing the given incident electron energy by the number of electrons produced during the slowing, including all secondaries. The calculated values are shown in Fig. 10. Both models show excellent agreement for energies above about 60 eV. The asymptotic W value (for high incident energies) is 25.4 eV in both models. At energies below 60 eV, both models do not coincide as well due to the different partitioning of ionization and excitation levels at low incident energies.

The last simulated microdosimetric quantity is the slab penetration. Here the relative number (fraction) of electrons that penetrate liquid-water slabs of different thicknesses is calculated and displayed in Fig. 11 for incident electron energies of 10 keV and 100 keV. For a given number of incident electrons, the number of electrons leaving a slab of a given thickness is counted. The fraction starts to be larger than 1.0 (or 100%) due to the secondary electrons produced that are able to leave thin slabs. With increasing thickness of the slabs, the number of electrons declines until all are slowed inside the slab. As seen in Fig. 11a, somewhat greater penetration is found with NOREC. This can be attributed to the slightly different stopping powers in both codes (as shown and discussed in Fig. 9) and to the slight differences in the angular distributions of the primary inelastic event (see Fig. 8). For water vapor, Paretzke (2) calculated the 5% transmission range; i.e., the slab thickness through which the relative number of electrons exiting is 5% of the number of the normally incident electrons. With scaling for densities, he found good agreement with electron ranges in air and plastic obtained experimentally (48). However, we expect smaller values for the 5% transmission ranges in liquid water than in water vapor because energy is deposited at shorter distances in liquid water be-

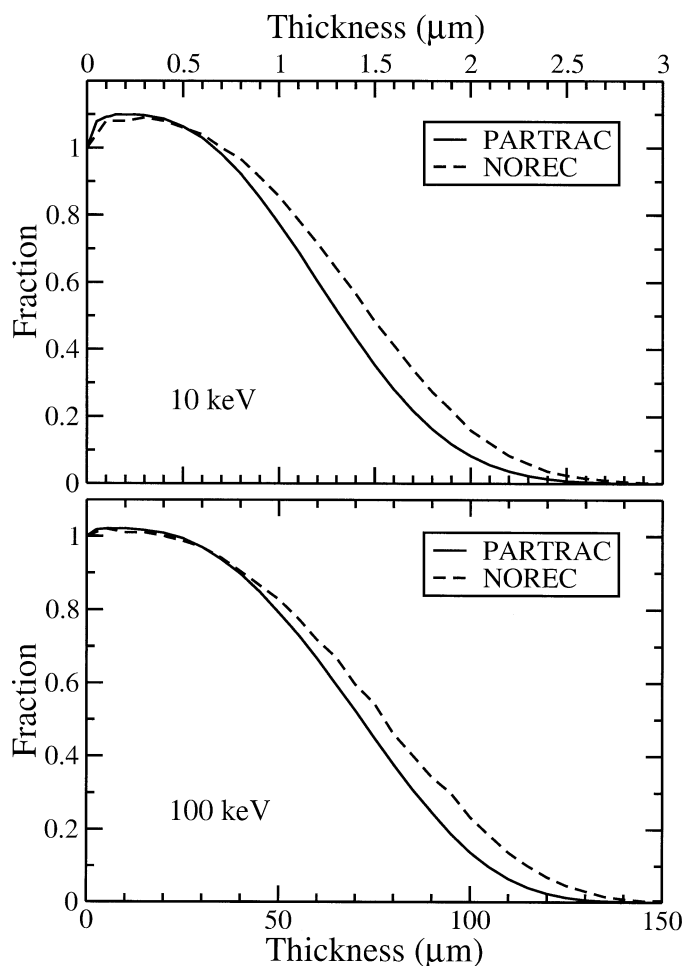


FIG. 11. Slab penetration. Shown is the relative number of electrons that exit a slab of thickness shown by the abscissa per normally incident electron (top panel: 10 keV kinetic energy, bottom panel: 100 keV kinetic energy).

cause of the somewhat shorter mean free path and larger G value in liquid water, as discussed elsewhere (19). In fact, we obtain 2.13 μm and 2.34 μm for 10 keV electrons for PARTRAC and NOREC, respectively, and 112.9 μm and 124.0 μm for 100 keV electrons. The values reported by Cole (48) are 3.1 μm (measured) and 2.9 μm (calculated) for 10 keV electrons and 163 μm (calculated) for 100 keV electrons. For comparison, ranges obtained within the continuous slowing down approximation for liquid water are 2.51 μm for 10 keV electrons and 143.1 μm for 100 keV electrons (20).

DISCUSSION

We note that the input data for inelastic interactions used in NOREC were chosen some time ago [see ref. (4) and references therein] and were based on the dielectric response function concept with connections to available experimental data at that time. More recent work (7) has evaluated differential inverse mean free path values that are also based on the dielectric response function but are deduced

from different and more detailed assumptions about the contributions from the different molecular orbitals to the response function.

It is gratifying that overall theoretical results for swift electron penetration in liquid water differ little when computed from NOREC and PARTAC. At this juncture it is not clear whether these are due to differences in input data or to nonlocality effects (e.g., plasmon excitation, thermalization of electrons at the track ends, transport at energies below 10 eV) included in parts in NOREC and PARTRAC. We are planning to extend our approach in NOREC to include (1) a detailed evaluation of the effects of nonlocal interactions, (2) a more detailed representation of contributions from molecular orbitals to the dielectric function, (3) a more accurate representation of angular distributions of scattered electrons as determined from $\epsilon(\omega, k)$, and (4) estimates of the contribution of intrinsic excitations to energy loss. We are planning to extend our approach in PARTRAC to (1) modify our model of the energy loss function to account for a better momentum dependence and new measurements (Sendai data), (2) include a more accurate representation of angular distributions (elastic and inelastic) of scattered electrons, and (3) include a better description of low-energy electrons (Sherbrooke data).

ACKNOWLEDGMENTS

This work is supported in part by NASA (grant NNJ04HF39G) and NIH/NCI (grant 2 R01 CA093351-04A1) (MD).

Received: April 24, 2007; accepted: January 10, 2008

REFERENCES

1. H. G. Paretzke, Radiation track structure theory. In *Kinetics of Non-homogeneous Processes* (G. R. Freeman, Ed.), pp. 89–170. Wiley, New York, 1987.
2. H. G. Paretzke, *Simulation von Elektronenspuren im Energiebereich 0.01–10 keV in Wasserdampf*. Report No. 24/88, GSF – National Research Center for Health and Environment, Neuherberg, Germany, 1988. [in German]
3. R. N. Hamm, H. A. Wright, R. H. Ritchie, J. E. Turner and T. P. Turner, Monte Carlo calculation of transport of electrons through liquid water. In *Proceedings of the 5th Symposium on Microdosimetry* (J. Booz, H. G. Ebert and B. G. R. Smith, Eds.), pp. 1037–1050. Commission of the European Communities, Luxembourg, 1975.
4. R. H. Ritchie, R. N. Hamm, J. E. Turner, H. A. Wright and W. E. Bolch, Radiation interactions and energy transport in the condensed phase. In *Physical and Chemical Mechanisms in Molecular Radiation Biology* (W. A. Glass and M. N. Varma, Eds.), pp. 99–133. Plenum Press, New York, 1991.
5. H. G. Paretzke, J. E. Turner, R. N. Hamm, H. A. Wright and R. H. Ritchie, Calculated yields and fluctuations for electron degradation in liquid water and water vapor. *J. Chem. Phys.* **84**, 3182–3188 (1986).
6. H. Nikjoo, S. Uehara, D. Emfietzoglou and F. A. Cucinotta, Track-structure codes in radiation research. *Radiat. Meas.* **41**, 1052–1074 (2006).
7. M. Dingfelder, D. Hantke, M. Inokuti and H. G. Paretzke, Electron inelastic-scattering cross sections in liquid water. *Radiat. Phys. Chem.* **53**, 1–18 (1998).
8. V. A. Semenenko, J. E. Turner and T. B. Borak, NOREC, a Monte

- Carlo code for simulating electron tracks in liquid water. *Radiat. Environ. Biophys.* **42**, 213–217 (2003).
9. J. M. Heller, Jr., R. N. Hamm, R. D. Birkhoff and L. R. Painter, Collective oscillations in liquid water. *J. Chem. Phys.* **60**, 3483–3486 (1974).
 10. Y. J. Xu, G. S. Khandelwal and J. W. Wilson, Proton stopping cross sections of liquid water. *Phys. Rev. A* **32**, 629–632 (1985).
 11. C. D. Jonah, M. S. Matheson, J. R. Miller and E. J. Hart, Yield and decay of the hydrated electron from 100 ps to 3 ns. *J. Phys. Chem.* **80**, 1267–1270 (1976).
 12. J. Daniels, C. V. Festenburg, H. Raether and K. Zeppenfeld, Optical constants of solids by electron spectroscopy. *Springer Tracts Mod. Phys.* **54**, 77–135 (1970).
 13. K. Siegbahn, C. Nordling, G. Johansson, J. Hedman, P. F. Hedén, K. Hamrin, U. Gelius, T. Bergmark and L. O. Werme, *ESCA Applied to Free Molecules*. North-Holland, Amsterdam, 1969.
 14. K. H. Tan, C. E. Brion, P. E. Van der Leeuw and M. J. van der Wiel, Absolute oscillator strengths (10–60 eV) for the photoabsorption, photoionisation and fragmentation of H₂O. *Chem. Phys.* **29**, 299–309 (1978).
 15. C. J. Tung, R. H. Ritchie, J. C. Ashley and V. E. Anderson, *Inelastic Interactions of Swift Electrons in Solids*. Report ORNL-TM-5188, Oak Ridge National Laboratory, Oak Ridge, TN, 1976.
 16. L. D. Landau and E. M. Lifshitz, *Electrodynamics of Continuous Media*. Pergamon Press, London, 1970.
 17. D. Pines and P. Nozières, *The Theory of Quantum Liquids*. W. A. Benjamin, New York, 1966.
 18. R. H. Ritchie, R. N. Hamm, J. E. Turner and H. A. Wright, The interaction of swift electrons with liquid water. In *Proceedings of the Sixth Symposium on Microdosimetry* (J. Booz and H. G. Ebert, Eds.), pp. 345–354. Harwood Academic Publishers, London, 1978.
 19. M. Dingfelder and W. Friedland, Basic data for track structure simulations: Electron interaction cross sections in liquid water. In *Advanced Monte Carlo for Radiation Physics, Particle Transport Simulations and Applications* (A. Kling, F. Barão, M. Nagagawa, L. Távorá and P. Vaz, Eds.), pp. 267–272. Springer Verlag, Berlin, 2001.
 20. ICRU, *Stopping Powers for Electrons and Positrons*. Report No. 37, International Commission on Radiation Units and Measurements, Bethesda, MD, 1984.
 21. H. Bichsel and T. Hiraoka, Energy loss of 70 MeV protons in elements. *Nucl. Instrum. Methods B* **66**, 345–351 (1992).
 22. M. Dingfelder and M. Inokuti, The Bethe surface of liquid water. *Radiat. Environ. Biophys.* **38**, 93–96 (1999).
 23. F. Ballarini, M. Biaggi, M. Merzagora, A. Ottolenghi, M. Dingfelder, W. Friedland, P. Jacob and H. G. Paretzke, Stochastic aspects and uncertainties in the prechemical and chemical stages of electron tracks in liquid water: a quantitative analysis based on Monte Carlo simulations. *Radiat. Environ. Biophys.* **39**, 179–188 (2000).
 24. N. Watanabe, H. Hayashi and Y. Udagawa, Bethe surface of liquid water determined by inelastic x-ray scattering spectroscopy and electron correlation effects. *Bull. Chem. Soc. Jpn.* **70**, 719–726 (1997).
 25. H. Hayashi, N. Watanabe, Y. Udagawa and C. C. Kao, Optical spectra of liquid water in vacuum uv region by means of inelastic x-ray scattering spectroscopy. *J. Chem. Phys.* **108**, 823–825 (1998).
 26. H. Hayashi, N. Watanabe, Y. Udagawa and C. C. Kao, The complete optical spectrum of liquid water measured by inelastic x-ray scattering. *Proc. Natl. Acad. Sci. USA* **97**, 6264–6266 (2000).
 27. N. Watanabe, H. Hayashi and Y. Udagawa, Inelastic X-ray scattering study on molecular liquids. *J. Phys. Chem. Solids* **61**, 407–409 (2000).
 28. D. Emfietzoglou and H. Nikjoo, The effect of model approximations on single-collision distributions of low-energy electrons in liquid water. *Radiat. Res.* **163**, 98–111 (2005).
 29. D. Emfietzoglou, F. A. Cucinotta and H. Nikjoo, A complete dielectric response model for liquid water: A solution of the Bethe ridge problem. *Radiat. Res.* **164**, 202–211 (2005).
 30. D. Emfietzoglou and H. Nikjoo, Accurate electron inelastic cross sections and stopping powers for liquid water over the 0.1–10 keV range based on an improved dielectric description of the Bethe surface. *Radiat. Res.* **167**, 110–120 (2007).
 31. B. Boudaïffa, P. Cloutier, D. Hunting, M. A. Huels and L. Sanche, Resonant formation of DNA strand breaks by low-energy (3 to 20 eV) electrons. *Science* **287**, 1658–1660 (2000).
 32. X. Pan, P. Cloutier, D. Hunting and L. Sanche, Dissociative electron attachment to DNA. *Phys. Rev. Lett.* **90**, 208102 (2003).
 33. F. Martin, P. D. Burrow, C. Zhongli, P. Cloutier, D. Hunting and L. Sanche, DNA strand breaks induced by 0–4 eV electrons: The role of shape resonances. *Phys. Rev. Lett.* **93**, 068101 (2004).
 34. X. Pan and L. Sanche, Mechanism and site of attack for direct damage to DNA by low-energy electrons. *Phys. Rev. Lett.* **94**, 198104 (2005).
 35. Y. Zheng, J. R. Wagner and L. Sanche, DNA damage induced by low-energy electrons: electron transfer and diffraction. *Phys. Rev. Lett.* **96**, 208101 (2006).
 36. R. Panajotovic, F. Martin, P. Cloutier, D. Hunting and L. Sanche, Effective cross sections for production of single-strand breaks in plasmid DNA by 0.1 to 4.7 eV electrons. *Radiat. Res.* **165**, 452–459 (2006).
 37. S. Ptasíńska and L. Sanche, Dissociative electron attachment to hydrated single DNA strands. *Phys. Rev. E* **75**, 031915 (2007).
 38. L. Sanche, Low energy electron-driven damage in biomolecules. *Eur. Phys. J. D* **35**, 367–390 (2005).
 39. M. Michaud, A. Wen and L. Sanche, Cross sections for low-energy (1–100 eV) electron elastic and inelastic scattering in amorphous ice. *Radiat. Res.* **159**, 3–22 (2003).
 40. J. Meesungnoen, J-P. Jay-Gerin, A. Filali-Mouhim and S. Mankhetkorn, Low-energy electron penetration range in liquid water. *Radiat. Res.* **158**, 657–660 (2002).
 41. Q-B. Lu, A. D. Bass and L. Sanche, Superinelastic electron transfer: electron trapping in H₂O ice via the N₂⁻(²I_g) resonance. *Phys. Rev. Lett.* **88**, 147601 (2002).
 42. M. J. Berger, S. M. Seltzer, R. Wang and A. Schechter, *Elastic Scattering of Electrons and Positrons by Atoms: Database ELAST*. Report NISTIR 5166, U.S. Department of Commerce, Gaithersburg, MD, 1993.
 43. S. Segui, M. Dingfelder and F. Salvat, Distorted-wave calculation of cross sections for inner-shell ionization by electron and positron impact. *Phys. Rev. A* **67**, 062710 (2003).
 44. C. B. Opal, E. C. Beatty and W. K. Peterson, *Tables of Energy and Angular Distributions of Electrons Ejected from Simple Gases by Electron Impact*. Report No. 108, Joint Institute for Laboratory Astrophysics (JILA), Boulder, CO, 1971.
 45. C. B. Opal, E. C. Beatty and W. K. Peterson, Tables of secondary electron production cross sections. *Atomic Data* **4**, 209 (1972).
 46. IAEA, *Atomic and Molecular Data for Radiotherapy and Radiation Research*. Report IAEA-TECDOC-799, International Atomic Energy Agency, Vienna, 1995.
 47. ICRU, *Fundamental Quantities and Units for Ionizing Radiation*. Report No. 60, International Commission on Radiation Units and Measurements, Bethesda, MD, 1998.
 48. A. Cole, Absorption of 20-eV to 50,000-eV electron beams in air and plastic. *Radiat. Res.* **39**, 7–33 (1969).